Title

Atomic Structures of Anthrax Prechannel Bound with Full-Length Lethal and Edema Factors

Journal

Structure, 28(8)

ISSN

0969-2126

Authors

Zhou, Kang
Liu, Shiheng
Hardenbrook, Nathan J
et al.

Publication Date

2020-08-01

DOI

10.1016/j.str.2020.05.009

Peer reviewed

HHS Public Access

Author manuscript

Structure. Author manuscript; available in PMC 2021 August 04.

Published in final edited form as:

Structure. 2020 August 04; 28(8): 879–887.e3. doi:10.1016/j.str.2020.05.009.

Atomic structures of anthrax prechannel bound with full-length lethal and edema factors

Kang Zhou[1,4], **Shiheng Liu**[1,2,4], **Nathan J. Hardenbrook**[3,4], **Yanxiang Cui**[1], **Bryan A. Krantz**[3,*], **Z. Hong Zhou**[1,2,5,*]

[1]California NanoSystems Institute, University of California, Los Angeles, California, 90095, U.S.A

[2]Department of Microbiology, Immunology and Molecular Genetics, University of California, Los Angeles, California, 90095, U.S.A.

[3]Department of Microbial Pathogenesis, University of Maryland, Baltimore, Baltimore, Maryland, 21201, U.S.A.

[4]These authors contributed equally to this work.

[5]Lead Contact.

Summary

Pathogenesis of anthrax disease involves two cytotoxic enzymes—edema factor (EF) and lethal factor (LF)—which are individually recruited by the protective antigen heptamer (PA_7) or octamer (PA_8) prechannel and subsequently translocated across channels formed on the endosomal membrane upon exposure to low pH. Here, we report the atomic structures of PA_8 prechannel-bound full-length EF and LF. In this pre-translocation state, the N-terminal segment of both factors refolds into an α helix engaged in the α clamp of the prechannel. Recruitment to the PA prechannel exposes an originally buried β strand of both toxins and enables domain organization of EF. Many interactions occur on domain interfaces in both PA prechannel-bound EF and LF, leading to toxin compaction prior to translocation. Our results provide key insights into the molecular mechanisms of translocation-coupled protein unfolding and translocation.

Graphcial Abstract

[*]To whom correspondence should be addressed. Z. Hong Zhou, hong.zhou@ucla.edu, Or Bryan A. Krantz, bkrantz@umaryland.edu.
Author contributions: Z.H.Z. and B.K. conceived the project; N.J.H. engineered and isolated samples; K.Z. and S.L. evaluated the samples, performed cryoEM, processed the data, built atomic models and prepared figures; Y.C. helped with cryoEM; Z.H.Z., K. Z. and S.L. interpreted the data and wrote the paper; all authors edited and approved the paper.

Declaration of interests: The authors declare no competing interests.

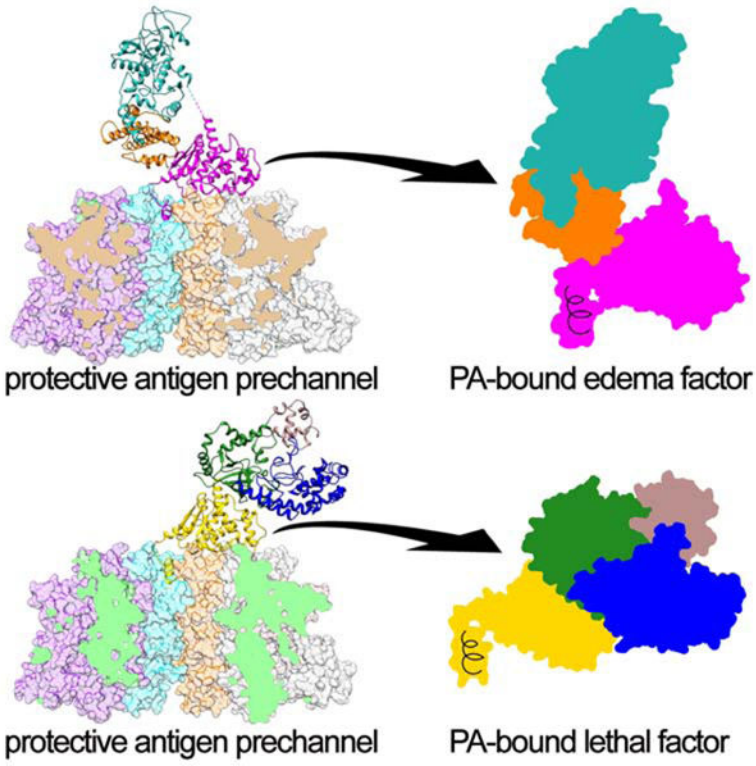

Introduction

Anthrax is an ancient and deadly disease caused by the spore-forming bacterial pathogen *Bacillus anthracis* (Doganay and Demiraslan, 2015; Pavan et al., 2011). Today, anthrax mostly affects wildlife and livestock, though it remains a major public health concern, particularly among people who handle contaminated animal products (Pohanka, 2019). More significantly, the month-long 2001 anthrax attacks that occurred one week after the September 11 terrorist attacks have resulted in public awareness of anthrax as a bioterrorism threat (Kalamas, 2004). Among the tier 1 biological select agents and toxins of the United States Federal Select Agent Program enacted since the September 11 attacks, *B. anthracis* is of particular concern due to the high resilience of its spores, high fatality rate and the lack of a civilian vaccination program.

Anthrax toxin inflicts harm on the host only after translocation across host cell membranes. Protein translocation consists of two steps: recruitment of a cytotoxic enzyme to the cell surface accompanied by partial unfolding and threading of the enzyme through the narrow conduit of a translocon, which spans the host cell membrane (Ho et al., 2018; Krantz et al., 2006; Matouschek, 2003; Wickner and Schekman, 2005; Zhang et al., 2004). Specific to anthrax, two enzyme factors, edema factor (EF, 89 kDa) and lethal factor (LF, 91 kDa) are translocated by the membrane protein protective antigen (PA, 83 kDa). PA undergoes furin cleavage to form a ring-shaped homo-oligomeric prechannel, either a heptamer (PA_7) or an octamer (PA_8) (Kintzer et al., 2009), which recruit EF and LF to form a complex, where the EF and LF are bound in a partially unfolded state. Both the PA_7 and PA_8 prechannel

complexes are physiologically relevant, as they both have been extracted from host cells at a 2:1 ratio (Kintzer et al., 2009). Further work done assembling PA oligomers in a physiological pH of 7.3 in bovine serum favors the formation of PA_8 (Kintzer, et al 2010). In this same environment, PA_7 is unstable and prone to premature conversion to the channel state, resulting in aggregation (Kintzer et al., 2009). Either the PA_7 or PA_8 complex is then endocytosed by the host cell. Within the endosomal compartment, the acidic environment induces a conformational change in the PA prechannel, resulting in the formation of a β-barrel channel that inserts itself into the endosomal membrane (Jiang et al., 2015). A proton gradient formed between the endosome and the cytosol provides the energy source to drive the translocation process (Krantz et al., 2006). The bound EF or LF is also destabilized by the acidic environment within the endosome, facilitating its unfolding and translocation through the channel (Krantz et al., 2004).

Atomic structures of the PA prechannel (Feld et al., 2010; Kintzer et al., 2009; Lacy et al., 2004; Petosa et al., 1997; Santelli et al., 2004) and channel (Jiang et al., 2015) have been determined by X-ray crystallography (Feld et al., 2010; Kintzer et al., 2009; Lacy et al., 2004) and cryo electron microscopy (cryoEM) (Jiang et al., 2015), respectively, revealing structural features of PA supporting translocation. For example, the PA monomer has a four-domain organization and oligomerizes into a ring-shaped structures with a negatively charged lumen (Petosa et al., 1997). The PA channel contains three polypeptide clamps (Thoren and Krantz, 2011): the α clamp (Feld et al., 2010), the ϕ clamp (Krantz et al., 2005), and the charge clamp (Wynia-Smith et al., 2012). The α clamps, found on the topmost surface of PA, are clefts formed between two PA subunits that binds to α helices non-specifically (Feld et al., 2010). Directly below the α clamp within the center of the channel is the ϕ clamp. The 2.9-Å resolution cryoEM structure of the PA channel reveals that the ϕ clamp forms a constricted 6-Å bottleneck where Phe427 residues from each of the PA protomers converge (Feld et al., 2010; Jiang et al., 2015). Below the ϕ clamp is a charge clamp formed by the transmembrane β-barrel (Wynia-Smith et al., 2012). As the partially protonated polypeptide chain moves from the lower pH in the endosome towards the higher pH within the cytosol, it passes the negatively charged acidic residues of the clamp. The inner diameter of the channel spans a range of diameters as small as 20 Å, wide enough to accommodate α helix in the translocating peptide, but not large enough to fit fully folded domains of the enzyme factors. Atomic structures of LF alone (Pannifer et al., 2001) and of EF bound with calmodulin (CaM) (Drum et al., 2002) have also been solved by crystallography. The PA prechannel in complex with the truncated N-terminal domain of LF has also been elucidated by crystallography (Feld et al., 2010). However, in the absence of high-resolution structures of the full-length cytotoxic enzymes in complex with PA prechannel, the detailed mechanisms of how these two different enzymes with dissimilar architectures are recruited to PA are unknown. In addition, EF is known to be a calmodulin-activated adenylyl cyclase, whose function highly depends on CaM (Drum et al., 2002; Shen et al., 2005), it is unclear whether and how EF interacts with CaM during EF's interplay with PA.

To gain insights into these questions, here we took advantage of convenience afforded by 4-fold symmetry in PA_8-toxin complexes to determine high-resolution structures and have determined the cryoEM structures of the PA_8 prechannel bound to full-length LF and EF.

These high-resolution structures of the PA prechannel with partially unfolded protein toxin factors reveal conformational changes occurring within the enzymatic factors, providing key insight into the mechanism of toxin recruitment prior to translocation.

Results

Structure of the PA octamer prechannel in complex with EF

Although X-ray crystallography has solved the PA octamer prechannel structure (Feld et al., 2010), as well as the EF-calmodulin (EF-CaM) structure (Shen et al., 2005), how EF binds to PA prechannel and how it effects translocation are both unknown. To gain insight into these questions, we set out to determine the structure of PA prechannel-EF complex by singe-particle cryoEM. Though both PA heptamer (PA_7) and octamer (PA_8) are known to translocate toxins effectively (Kintzer et al., 2009), PA_8 was chosen in this study because, unlike PA_7, the available substrate binding space on PA_8 prechannel could accommodate up to four EF subunits simultaneously, potentially facilitating image processing. Since EF may dissociate from prechannel during purification, we used a symmetry expansion method for 3D classification and classified the particles into classes with different numbers of bound EF subunits (Methods, Figure S2). Our subsequent structural refinement and atomic modeling focuses on the class with four EF bound, thanks to its large number of particles permitting high-resolution analysis.

The cryoEM structure of EF in complex with PA_8 prechannel has an average resolution of 3.3 Å (Figure 1A and Figure S3, A-C). Though the local resolutions vary, PA_8 prechannel and the regions of the bound EF involved in PA-EF interactions have the highest resolution, enabling us to build atomic models for these regions (Figure 1, B and C). The structure of the complex has a “flowers-in-vase” appearance: the vase corresponds to the octameric PA prechannel and the flowers to the four EF molecules “plugged” into the vase (Figure 1, A and C, and movie S1). Viewed from top, the four EF “flowers” are distributed symmetrically like a rhombus, but there are no direct interactions between any two EF molecules in the complex (Figure 1B). Each EF subunit occupies binding surfaces from two neighboring PA subunits with its “flower stem” plugged into top of the PA_8 prechannel (Figure 1, C and D, and movie S1).

The PA_8 prechannel structure in the PA_8 prechannel-EF_4 complex is the same as the reported crystal structure of PA_8 prechannel (Feld et al., 2010). The structure of the full-length EF subunit in the complex consists of three domains: PA binding domain (PABD), adenylate cyclase domain (ACD) and helical domain (HD) (Figure 2A). Among the three domains of PA_8-bound EF, only PABD has direct interactions with PA prechannel, one with its α-clamp and the other with its domain 1 (Figure 1D). The N-terminal residues (Lys20 to Thr42) of PABD form an α helix (α1) and a loop, which docks into the α-clamp of PA prechannel (Figure 1D and Figure 2B). In addition to the α-clamp engaged interactions, another hydrophobic interface is formed between domain 1 of PA prechannel and PABD of EF (Figure 1D). Following the PABD, ACD projects far away from PA prechannel while HD traces back towards the PA prechannel (Figure 2B), shaping EF into a triangular flower with its stem held by α-clamp of the PA prechannel (Figure 2B).

The only known structure of full-length EF is that in the EF-CaM complex solved by crystallography (Shen et al., 2005). In this CaM-bound EF structure, the three domains of EF are linked by two long loops and have no direct domain interactions (Figure 2C), hinting that the apo-EF may exists in a relatively flexible state without CaM bound. On the other hand, CaM is necessary for EF's activity as a calmodulin-activated adenylyl cyclase, indicating that the CaM-bound EF structure is a functional conformation *in vivo* (Drum et al., 2002). For these reasons, we can only compare our PA_8-bound EF with the CaM-bound EF structure.

Our comparison reveals two remarkable differences between PA_8-bound EF and CaM-bound EF. First, as mentioned above, the N-terminal residues (Lys20 to Thr42) of PABD form an α helix (α1) and a loop. However, in the CaM-bound EF structure (Shen et al., 2005), Lys20-Ile30 are invisible while Asn31-Thr42 form a β strand and a loop (Figure 2C). Second, in CaM-bound EF structure (PDB: 1XFY) (Shen et al., 2005), CaM binds to adenylate cyclase domains (ACD) and the helical domain (HD) of EF simultaneously, and no significant interactions among these EF domains are observed (Figure 2C). While in the PA_8-bound EF structure, the HD domain contributes to a new conformation by bridging PABD and ACD (Figure 2B). Further analysis indicates that the fold of individual domains remains the same from CaM-bound EF to PA_8-bound EF, but the three domains are reorganized in the PA_8-bound EF (Figure 2D). In detail, on one side of the HD, residues near α29 and α30 of HD interact with those near α2 and β1 of the PABD (Figure 2B). On the other side of HD, a loop between α26 and α27 interacts with residues near α22 and α24 of ACD, mainly through inter-domain hydrogen bonds (Figure 2B). With the extensive interactions mentioned above, HD moves towards and binds PABD eventually. Notably, refolding of the N-terminal residues (Lys20 to Thr42) of PABD eventually yields the space that enables the interactions between HD and PABD (orange arrow in Figure 2D). Together with movement of HD, after a ~60° swing (cyan arrow in Figure 2D), ACD mounts its α22 and α24 helices on the HD regions near α25, α26 and α27 helices (Figure 2B).

Structure of the PA octamer prechannel in complex with LF

Unlike EF, LF is a protease that cleaves and disables the mitogen-activated protein kinase kinase (MAPKK) family of proteins. The crystal structure of PA_8 prechannel in complex with the N-terminal domain of LF (LF_N) showed how the first α-helix and β strand of LF_N unfolded and docked into the α clamp of prechannel (Feld et al., 2010), but our mechanistic understanding of toxin recruitment remains incomplete in the lack of the prechannel structure bound to full-length LF. A prior cryoEM study has documented that, when full-length LF is recruited to the PA prechannel, the N-terminal domain of one LF subunit contacts the C-terminal domain of the neighboring LF subunit (Fabre et al., 2016); however, the low resolution (16Å) of the cryoEM map was insufficient to reveal the biochemical nature of these contacts. Here, using similar data-processing workflow as that for PA_8-EF, we obtained a cryoEM density map of full-length LF in complex with the PA_8 prechannel at an average resolution of 3.8 Å, enabling us to build atomic models for regions involved in PA-LF interactions and adjacent LF interactions (Figure 1E and Figure S3, D-F).

The overall structure of PA_8 prechannel-LF_4 shares the "flowers-in-vase" appearance of the above described PA_8 prechannel-EF_4 complex (Figure 1, E and G, and movie S2). The vase corresponds to the octameric PA prechannel and the flowers to the four LF molecules "plugged" into the vase (Figure 1G). Viewed from top, the four LF "flowers" are distributed symmetrically a square rather than a rhombus of EFs. (Figure 1F). Similar to the situation of PA_8 prechannel-bound EF, each LF subunit occupies binding surfaces from two neighboring PA subunits with its "flower stem" plugged into top of the PA_8 prechannel (Figure 1, G and H, and movie S2).

In our PA8-full-length LF complex (Figure 2, A and E), each LF has four domains including PA binding domain (PABD), VIP2 like domain (VIPD), helix bundle domain (HBD) and catalytic center domain (CCD) (Figure 2A). The PABD structures in PA_8 prechannel-LF and the previous PA_8 prechannel-LF_N (Feld et al., 2010) are similar. Likewise, the N-terminal residues (Asn29-Glu47) of LF refold into an α helix (α1)-loop configuration (Figure 2E) docking into the α-clamp of PA_8. Prior to this refolding, these residues were in an α helix/β-strand configuration in the apo-form LF (Figure 2F). This refolding of N-terminal residues happens in both LF and EF and plays critical role in PA binding, though the conformations of the two N-terminal α helices (α1) from LF and EF are not the same, as discussed below.

Besides the N-terminal residues of LF, other residues of PABD, including Try108, Leu188, Tyr223 and Val232, interact with PA prechannel mainly through hydrophobic interactions (Figure 1H). Generally, the interactions between PA prechannel and the PABD in either EF or LF are similar. Nevertheless, in contrast to the domain reorganization observed in EF, comparison between PA_8-bound LF and apo-form LF reveals no conformational change upon PA prechannel binding, except for the refolding of the N-terminal residues (Figure 2F). In addition, every LF molecule has interactions with its neighboring LF, while no interactions between neighboring EFs are observed in PA_8 prechannel-EF_4 complex, as discussed later.

Comparison of prechannel-bound EF and LF reveals shared features in their pre-translocation state

EF and LF are very different cytotoxic enzymes: the former is a Ca^{2+} and calmodulin-activated adenylyl cyclase while the latter is a protease belonging to the Zn^{2+} metalloprotease family. As such, EF and LF have no functional similarity, but both are translocated by PA. Comparison of PA_8 prechannel-EF_4 with PA_8 prechannel-LF_4 structures thus provides an opportunity to identify the shared features that are likely required for pre-translocation of anthrax toxins.

Comparisons of EF and LF structures in their prechannel-bound state with those in the prechannel-unbound state (*i.e.*, LF alone and CaM-bound EF) reveal that the refolding of N-terminal residues in PABD domain is a shared conformational change (Figure 2, D and F), which was thought to be important for preparing polypeptide translocation (Feld et al., 2010). Remarkably, the amino acid sequences of the PABD in EF and LF are conserved (38% identities) (Figure 3E), especially for those residues involved in the hydrophobic interactions with PA. PABD-aligned superposition between prechannel-bound EF and LF also shows that the overall structure of the two PABDs are very similar (Figure 3A). Despite

these similarities, this superposition reveals that the N-terminal α-helices (α1) of EF and LF are not in the same conformation. The α1 of EF shifts upwards about 25° (Figure 3, A and B), moreover, the sequences of α1 share no similarity compared to the full PABD (38% identity). Beyond mutation analysis (Feld et al., 2010), our structures provide direct structural evidence to support the notion that the α-clamp of PA prechannel has plasticity in how it engages the different α helices from the enzymatic factors.

PA prechannel-bound EF undergoes a drastic domain reorganization. EF is a calmodulin-activated adenylyl cyclase whose activity depends on CaM binding, but it is unlikely that PA translocates CaM together with EF as CaM is not found outside mammalian cytosol. Unlike the extended structure of CaM-bound EF (Figure 2C), domain reorganization leads to overall structure compaction of EF in its PA-bound state.

Despite the observation that LF doesn't undergo the type of drastic domain movements of EF when it binds to PA prechannel, the β2 strands in their PABDs both maintain protein interactions, thus possibly contributing to the binding of toxins to PA prechannel. The β2 strand resides near the critical N-terminal α1 and its downstream loop in both enzymes (Figure 3A). The β2 strand of EF's PABD interacts with a loop of HD from the same EF subunit (Figure 3C), with no interaction between any neighboring EF molecules. In contrast, the β2 strand of LF's PABD also interacts with a loop, but this loop belongs to the CCD of a neighboring LF subunit (Figure 3D). We suggest that the interactions involving β2 probably help stabilize the LF/EF binding to the prechannel. Regardless whether enzyme domain reorganization occurs or not upon binding to PA prechannel, many compaction-promoting interactions were observed in both PA-bound EF and LF structures at their domain interfaces, suggesting that the compact overall structures of these enzymatic toxins are favorable for PA binding and subsequent translocation.

Discussion

Here, we report two cryoEM structures of PA_8 prechannel bound to the full-length enzyme substrates: the PA_8 prechannel-EF_4 complex structure at 3.3 Å resolution and the PA_8 prechannel-LF_4 complex structure at 3.8 Å resolution. Our results reveal that, upon binding to the PA prechannel, conformational changes occur in both EF and LF, but the detailed structural remodeling is not identical. Compared to the CaM-bound EF structure, two significant conformational changes are observed in the EF structure. First, the N-terminal residues (Lys20 to Thr42) of the PABD refold from a β-strand to an α helix and a loop that dock- in the α-clamp of PA prechannel. Second, the domains of EF reorganize involving a 70° swing of HD towards PABD and mounting of ACD to HD. The refolding of the N-terminus of the PABD yields the space for HD movement, and exposes the β2 strand that interacts with a loop of the swung HD. In the case of LF, only the refolding of N-terminal residues occurs, with the rest of the structure remaining the same as the apo-form of LF. Thus, the refolding of the N-terminal residues of LF and EF is a shared feature of these two very different cytotoxic enzymes. In the previous study, Feld et al. showed that different amino acid sequences bind to the α-clamp (Feld et al., 2010); the structures presented here give direct structural evidence revealing that the α-clamp of the PA prechannel engages the α helix of both enzyme factors. Furthermore, EF and LF have no functional similarity but

both are translocated by PA due to their similar PABD domains. Most residues of the PABD of EF and LF involved in prechannel binding are well conserved. A comparison of the PABD of EF and LF draws attention to the β2 strand, which is near the critical N-terminal α1 and a loop. The β2 strand interacts with a loop from the HD of the same EF in the PA_8 prechannel-EF_4 structure, while the β2 strand interacts with a loop from the CCD of the neighboring LF in the PA_8 prechannel-LF_4 structure. Therefore, these β2 strand interactions may aid in PA prechannel binding.

Our PA_8 prechannel-EF_4 and PA_8 prechannel-LF_4 structures are the first structures of full-length EF and LF complexed with a PA prechannel, and they provide further insight into the mechanism of how PA prechannel recruits the enzyme factors and primes them for translocation (Figure 4). Before binding to the PA prechannel, EF reorganizes and refolds to adapt the prechannel entrance at the α-clamp (Figure 4). For LF, the apo structure is relatively compact, therefore no major conformational changes are needed for PA binding. Subsequently, when EF or LF binds to PA prechannel, the N-terminal residues of PABD are induced to adapt α helix/loop configuration, which directly docks into the α-clamp of PA prechannel. Moreover, this refolding exposes the β2 strand, which makes it possible for β2 either to interact with loop from the same EF in PA_8-EF complex or to interact with loop from a neighboring LF in PA_8-LF complex. In both EF and LF, these interactions may help to recruit the cytotoxic enzymes. The tight binding space for toxin factors on the PA prechannel may imply that, a compact and ordered conformation of LF/EF is favorable for PA binding and more effective recruitment.

In summary, these structural studies of EF and LF bound to the PA prechannel provide key insights into the molecular mechanism of target recruitment in the pre-translocation state. The molecular mechanism involves partial protein unfolding, domain reorganization and binding. Moving forward, these types of mechanisms found in anthrax toxin can be studied in similar systems, such as *Clostridum diffifcile* CtdB toxin (Krantz et al, 2005). Similarly, in another translocation model system, structures of the SecY translocon have been determined using crystallography and cryoEM while engaging translocating substrate (Li et al, 2016, Ma et al, 2019). SecA has been shown to also contain a polypeptide clamp site above the SecY pore (Li et al, 2016). This clamp induces short β strand conformations in the translocating polypeptide, allowing it to interact in a sequence-independent manner similar to the α-clamp in PA (Ma et al, 2019). The atomic description of the robust α-clamp and the highly conserved PABD structures resolved in both complexes are valuable to engineering PABD-tagged proteins, which may target cells for medical applications (Bachran, Leppla, 2016). In addition, as early symptoms of inhalation anthrax infection mimic influenza, it is difficult to diagnose early (Borio, Frank, & Mani, 2001; Plotkin, Brachman, Utell, Bumford, & Atchison, 2002). These structures will allow for structure-based drug design of novel antitoxins to neutralize anthrax toxin that may decrease fatality rates in the case of inhalation anthrax (Huang et al., 2015).

STAR★METHODS

RESOURCE AVAILABILITY

Lead Contact—Further information and requests for resources and reagents should be directed to and will be fulfilled by the Lead Contact, Prof. Z. Hong Zhou (Hong.Zhou@ucla.edu).

Materials Availability

Plasmids and cells in this study are available from Prof. Bryan A. Krantz (bkrantz@umaryland.edu). All other materials generated are available from Prof. Z. H. Zhou (Hong.Zhou@ucla.edu).

Data and Code Availability

Coordinates and cryoEM density maps are available at the Protein Data Bank and the Electron Microscopy Data Bank under accession numbers PDB 6VRA, PDB 6WJJ, EMD-21365, EMD-21694.

EXPERIMENTAL MODEL AND SUBJECT DETAILS

E. coli BL21(DE3) strain has been used for the studies. The cells were grown in 10 L fermenters at 37 °C in ECPM1 broth. Additional details are provided in the Method Details section.

METHOD DETAILS

Protein Expression and Purification—Two mutants of PA—a D512K mutant (PA_{D512K}), and a K245G/R252N mutant ($PA_{G/N}$), which when mixed at a 1:1 ratio exclusively form octameric PA in the presence of substrate (Phillips et al., 2013)—were created using QuikChange II XL site-directed mutagenesis kits (Agilant Product Number 200251). In both mutants, the furin cleavage site was replaced with a 3C Protease cleavage site (Cordingley et al., 1990), allowing for assembly in the absence of trypsin (the protease that is typically used) degradation. These PA_{83} variants were recombinantly grown in pET22b vectors to express PA and traffic it to the periplasm, using *E. coli* BL21(DE3) cells as previously described. Bacteria were grown in 10 L fermenters at 37 °C in ECPM1 broth (Barnard and Payton, 1995). At an OD_{600} of ~4, expression was induced at 30 °C for 2 hours with isopropyl-β-D-thiogalactoside (IPTG) to a final concentration of 300 μM. Periplasmic lysis was performed by resuspending the pelleted bacterial cells in 20% (w/v) sucrose, 20 mM Tris pH 8, 1 mM ethylenediaminetetraacetic acid (EDTA). Bacteria were then pelleted and resuspended in 5 mM $MgSO_4$. The bacteria were pelleted a final time, and the supernatant was collected containing the periplasmic lysate. PA_{83} was further purified using Q-Sepharose anion-exchange chromatography in 20 mM Tris, pH 8 and 20mM Tris pH 8, 1M NaCl. PA_{83} mutants were then cleaved using 3C Protease at a ratio of 20 U of 3C Protease to 1 mg PA (at 1 mg ml^{-1} PA concentration). This reaction was allowed to cleave overnight at 4 °C.

Recombinant LF and EF containing an amino-terminal His_6-tag were overexpressed in *E. coli* BL21(DE3) from pET15b constructs, and purified from the cytosol using His_6 affinity chromatography.

PA-LF and PA-EF complex assembly—After 3C Protease cleavage, 5 mg PA_{D512K} and 5 mg $PA_{G/N}$ were mixed with 10 mg of EF or LF (1:1 w/w), and diluted to 1 mg ml^{-1} total protein concentration (20 ml) in 20 mM Tris pH 8, 150 mM NaCl. This mixture was allowed to assemble overnight at 4 °C. The PA prechannel in complex with LF and EF was concentrated to 3–4 ml, and it was then purified over S400 gel filtration in 20 mM Tris pH 8, 150 mM NaCl. The sample was then concentrated to 0.87 mg ml^{-1} (PA_8 prechannel in complex with LF) and 1.05 mg ml^{-1} (PA_8 prechannel in complex with EF). Concentration was estimated by a Nanodrop spectrophotometer.

CryoEM sample preparation and imaging—For cryoEM sample optimization, an aliquot of 2.5 μl of sample was applied onto a glow-discharged holey carbon copper grid (300 mesh, QUANTIFOIL® R 2/1). The grid was blotted and flash-frozen in liquid ethane with an FEI Mark IV Vitrobot. An FEI TF20 cryoEM instrument was used to screen grids. CryoEM grids with optimal particle distribution and ice thickness were obtained by varying the time for glow discharge, the volume of applied samples, chamber temperature/humidity and blotting time/force.

Optimized cryoEM grids were loaded into an FEI Titan Krios electron microscope with a Gatan Imaging Filter (GIF) Quantum LS device and a post-GIF K2 Summit direct electron detector. The microscope was operated at 300 kV with the GIF energy-filtering slit width set at 20 eV. Movies were acquired with SerialEM (Mastronarde, 2005) by electron counting in super-resolution mode at a pixel size of 0.535 Å per pixel. A total number of 45 frames were acquired in 9 seconds for each movie, giving a total dose of ~60 $e^-/Å^2$/movie.

Drift correction of movie frames—Frames in each movie were aligned for drift correction with the graphics processing unit (GPU)-accelerated program MotionCor2 (Zheng et al., 2017). The first and last frame were discarded during drift correction. Two averaged micrographs, one with dose weighting and the other without dose weighting, were generated for each movie after drift correction. The averaged micrographs have a calibrated pixel size of 1.07 Å on the specimen scale. The averaged micrographs without dose weighting were used only for defocus determination and the averaged micrographs with dose weighting were used for all other steps of image processing.

Structure determination for the PA_8 prechannel in complex with either EF or LF—For the PA prechannel in complex with EF, the defocus value of each averaged micrograph was determined by CTFFIND4 (Rohou and Grigorieff, 2015) generating values ranging from −1.5 to 3 μm. Initially, a total of 1,010,953 particles were automatically picked from 4,353 averaged images without reference using Gautomatch (http://www.mrc-lmb.cam.ac.uk/kzhang). The particles were boxed out in dimensions of 256 × 256 square pixels before further processing by the GPU accelerated Relion v3.0 (Scheres, 2012). Several iterations of reference-free 2D classification were subsequently performed to remove bad particles (*i.e.*, classes with fuzzy or un-interpretable features), yielding 447,121 good

particles. These particles were submitted to cryoSPARC (Punjani et al., 2017) for an initial model. After one round of 3D classification with C8 symmetry, only the classes showing features corresponding to the intact PA_8 prechannel were kept, which contained 107,095 particles. These particles were applied one round of auto-refinement by RELION, yielding a map with an average resolution of 3.3 Å.

The EF binding sites in PA_8 prechannel were not fully occupied, thus we needed to perform symmetry mismatch classification to obtain the high-resolution map for EF. We expanded the good particles (intact PA_8 prechannel) from C8 symmetry to C1 (command : relion_particle_symmetry_expand), yielding 856,760 (107,095 × 8) particles. These particles were submitted to further classification (skip alignment) with 10 classes. A cylinder mask was created only for the EF binding region (Figure S2A) and applied for the focus classification. Among these 10 classes, two classes have no clear density of EF and 3 classes have density of four EF (Figure S2A). Subsequently, we selected the particles from classes with four EF. After removing duplications based on the unique particle names given by RELION, we obtained 78,465 particles for PA_8 prechannel-LF_4. These unique particles were subjected to a final step of 3D auto-refinement with C4 symmetry. The two half maps of each dataset from this auto-refinement step were subjected to RELION's standard post-processing procedure. The final map achieved 3.3 Å resolution based on RELION's gold-standard FSC (see below).

For the PA prechannel in complex with LF data set, the data processing workflow follows a similar way with PA_8 prechannel-EF_4 data set. Briefly, 593,079 raw particles were boxed out from 2,037 micrographs and binned to a pixel size of 2.14 Å. After rounds of 3D classification, 57,860 good particles with intact PA_8 prechannel were selected, yielding a 4.28 Å map with C4 symmetry (Figure S2B).

After the symmetry expansion from C4 to C1, 231,440 particles were generated and subjected to 'skip align' 3D classification of Relion requesting 6 classes. A tight mask covering all LF binding region were used during the symmetry mismatch classification. Only one good class (23,839 particles) containing four LFs was selected. These particles were finally subjected to a 3D auto-refinement with C4 symmetry and yield a map at 3.8 Å resolution (Figure S2B). All resolutions reported above are based on the "gold-standard" FSC 0.143 criterion. FSC curves were calculated using soft spherical masks and high-resolution noise substitution was used to correct for convolution effects of the masks on the FSC curves (Chen et al., 2013). Prior to visualization, all maps were sharpened by applying a negative B-factor which was estimated using automated procedures. Local resolution was estimated using Resmap (Swint-Kruse and Brown, 2005). The overall quality of the maps for the PA prechannel in complex with LF and EF is presented in Figure S3, respectively. Data collection and reconstruction statistics are presented in Table S1.

Model building and refinement—Atomic model building was accomplished in an iterative process involving Coot (Emsley and Cowtan, 2004), Chimera (Pettersen et al., 2004), and Phenix (Adams et al., 2010). For the PA channel in complex with EF, the structure of PA_8 prechannel octamer (Kintzer et al., 2009) (PDB: 3HVD) was fitted into the cryoEM map of PA_8 prechannel-EF_4 as initial model by using the 'fit in map' routine in

Chimera. This fit revealed the extra density corresponding to EF. However, further docking showed the density of EF in cryoEM map has significant differences with respect to the crystal structure of EF(Shen et al., 2005) (PDB ID: 1XFX). The full-length EF consists of 3 domains, the PA binding domain (PABD), adenylate cyclase domains (ACD), and the helical domain (HD). The domains in the cryoEM map have a different arrangement. Thus, we fit the three domains into the density separately to create an initial atomic model for PA_8 prechannel-EF_4, which was refined by 'real-space refinement' in Phenix (Adams et al., 2010). We then manually adjusted the main chain and side chains to match the cryoEM density map with Coot (Emsley and Cowtan, 2004). This process of real space refinement and manual adjustment steps was repeated until the peptide backbone and side chain conformations were optimized. Secondary structure, NCS restraints and geometry restraints were used during the refinement.

For the PA_8-LF complex, the structure of anthrax toxin PA prechannel octamer (Kintzer et al., 2009) (PDB: 3HVD) was fitted into the bottom of cryoEM map by using the 'fit in map' routine in Chimera. Then, the crystal structure of lethal factor (Pannifer et al., 2001) (PDB: 1J7N) was fitted in to the top of cryoEM map to create a full atomic model for the PA_8 prechannel-LF_4 complex. Finally, the structure was manually adjusted using Coot and refined using Phenix (Adams et al., 2010) in real space with secondary structure and geometry restraints.

Refinement statistics of the PA channel in complex with LF and EF are summarized in Table S1. These models were also evaluated based on MolProbity scores (Chen et al., 2010) and Ramachandran plots (Table S1). Representative densities for the proteins are shown in Figure S4. The cryoEM maps and atomic models were visualized using UCSF Chimera (Pettersen et al., 2004) and ChimeraX (Goddard et al., 2018).

QUANTIFICATION AND STATISTICAL ANALYSIS

All cryoEM data sets were processed using RELION (Figure S2 and Table S1). All resolutions reported are based on the "gold-standard" FSC 0.143 criterion (Figure S3). FSC curves were calculated using soft spherical masks and high-resolution noise substitution was used to correct for convolution effects of the masks on the FSC curves (Chen et al., 2013). Refinement statistics of all atomic models are summarized in Table S1. These models were also evaluated based on MolProbity scores (Chen et al., 2010) and Ramachandran plots.

Supplementary Material

Refer to Web version on PubMed Central for supplementary material.

Acknowledgments:

We thank I. Atanasov and W. Hui for assistance in cryoEM imaging. We thank R. J. Collier (Harvard Medical School) for providing the recombinant plasmids.

Funding: This work was supported in part grants from the National Science Foundation (NSF, under grant no. DMR-1548924) and by grants from the National Institutes of Health (R01GM071940/AI094386/DE025567 to Z.H.Z. and R21AI124020 to B.K.) and the Training Program in Integrative Membrane Biology at the University of Maryland, Baltimore (T32GM008181). We acknowledge the use of resources in the Electron Imaging Center for

Nanomachines supported by UCLA and grants from the NIH (S10RR23057, S10OD018111, and U24GM116792) and NSF (DBI-1338135). K.Z. acknowledges support from the China Scholarship Council.

References

Adams PD, Afonine PV, Bunkoczi G, Chen VB, Davis IW, Echols N, Headd JJ, Hung LW, Kapral GJ, Grosse-Kunstleve RW, et al. (2010). PHENIX: a comprehensive Python-based system for macromolecular structure solution. Acta Crystallogr D Biol Crystallogr 66, 213–221. [PubMed: 20124702]

Barnard A, and Payton M (1995). In Current Protocols in Protein Science. John Wiley & Sons, Inc Vol. 5.3, pp. 1–18.

Chen S, McMullan G, Faruqi AR, Murshudov GN, Short JM, Scheres SH, and Henderson R (2013). High-resolution noise substitution to measure overfitting and validate resolution in 3D structure determination by single particle electron cryomicroscopy. Ultramicroscopy 135, 24–35. [PubMed: 23872039]

Chen VB, Arendall WB 3rd, Headd JJ, Keedy DA, Immormino RM, Kapral GJ, Murray LW, Richardson JS, and Richardson DC (2010). MolProbity: all-atom structure validation for macromolecular crystallography. Acta Crystallogr D Biol Crystallogr 66, 12–21. [PubMed: 20057044]

Cordingley MG, Callahan PL, Sardana VV, Garsky VM, and Colonno RJ (1990). Substrate requirements of human rhinovirus 3C protease for peptide cleavage in vitro. J Biol Chem 265, 9062–9065. [PubMed: 2160953]

Doganay M, and Demiraslan H (2015). Human anthrax as a re-emerging disease. Recent Pat Antiinfect Drug Discov 10, 10–29. [PubMed: 25851429]

Drum CL, Yan SZ, Bard J, Shen YQ, Lu D, Soelaiman S, Grabarek Z, Bohm A, and Tang WJ (2002). Structural basis for the activation of anthrax adenylyl cyclase exotoxin by calmodulin. Nature 415, 396–402. [PubMed: 11807546]

Emsley P, and Cowtan K (2004). Coot: model-building tools for molecular graphics. Acta Crystallogr D Biol Crystallogr 60, 2126–2132. [PubMed: 15572765]

Fabre L, Santelli E, Mountassif D, Donoghue A, Biswas A, Blunck R, Hanein D, Volkmann N, Liddington R, and Rouiller I (2016). Structure of anthrax lethal toxin prepore complex suggests a pathway for efficient cell entry. J Gen Physiol 148, 313–324. [PubMed: 27670897]

Feld GK, Thoren KL, Kintzer AF, Sterling HJ, Tang II, Greenberg SG, Williams ER, and Krantz BA (2010). Structural basis for the unfolding of anthrax lethal factor by protective antigen oligomers. Nat Struct Mol Biol 17, 1383–1390. [PubMed: 21037566]

Goddard TD, Huang CC, Meng EC, Pettersen EF, Couch GS, Morris JH, and Ferrin TE (2018). UCSF ChimeraX: Meeting modern challenges in visualization and analysis. Protein Sci 27, 14–25. [PubMed: 28710774]

Ho CM, Beck JR, Lai M, Cui Y, Goldberg DE, Egea PF, and Zhou ZH (2018). Malaria parasite translocon structure and mechanism of effector export. Nature 561, 70–75. [PubMed: 30150771]

Jiang J, Pentelute BL, Collier RJ, and Zhou ZH (2015). Atomic structure of anthrax protective antigen pore elucidates toxin translocation. Nature 521, 545–549. [PubMed: 25778700]

Kalamas AG (2004). Anthrax. Anesthesiol Clin North Am 22, 533–540, vii. [PubMed: 15325717]

Kintzer AF, Thoren KL, Sterling HJ, Dong KC, Feld GK, Tang II, Zhang TT, Williams ER, Berger JM, and Krantz BA (2009). The protective antigen component of anthrax toxin forms functional octameric complexes. J Mol Biol 392, 614–629. [PubMed: 19627991]

Krantz BA, Finkelstein A, and Collier RJ (2006). Protein translocation through the anthrax toxin transmembrane pore is driven by a proton gradient. J Mol Biol 355, 968–979. [PubMed: 16343527]

Krantz BA, Melnyk RA, Zhang S, Juris SJ, Lacy DB, Wu Z, Finkelstein A, and Collier RJ (2005). A phenylalanine clamp catalyzes protein translocation through the anthrax toxin pore. Science 309, 777–781. [PubMed: 16051798]

Krantz BA, Trivedi AD, Cunningham K, Christensen KA, and Collier RJ (2004). Acid-induced unfolding of the amino-terminal domains of the lethal and edema factors of anthrax toxin. J Mol Biol 344, 739–756. [PubMed: 15533442]

Lacy DB, Wigelsworth DJ, Melnyk RA, Harrison SC, and Collier RJ (2004). Structure of heptameric protective antigen bound to an anthrax toxin receptor: a role for receptor in pH-dependent pore formation. Proc Natl Acad Sci U S A 101, 13147–13151. [PubMed: 15326297]

Mastronarde DN (2005). Automated electron microscope tomography using robust prediction of specimen movements. J Struct Biol 152, 36–51. [PubMed: 16182563]

Matouschek A (2003). Protein unfolding--an important process in vivo? Curr Opin Struct Biol 13, 98–109. [PubMed: 12581666]

Pannifer AD, Wong TY, Schwarzenbacher R, Renatus M, Petosa C, Bienkowska J, Lacy DB, Collier RJ, Park S, Leppla SH, et al. (2001). Crystal structure of the anthrax lethal factor. Nature 414, 229–233. [PubMed: 11700563]

Pavan ME, Pettinari MJ, Cairo F, Pavan EE, and Cataldi AA (2011). [Bacillus anthracis: a molecular look at a famous pathogen]. Rev Argent Microbiol 43, 294–310. [PubMed: 22274828]

Petosa C, Collier RJ, Klimpel KR, Leppla SH, and Liddington RC (1997). Crystal structure of the anthrax toxin protective antigen. Nature 385, 833–838. [PubMed: 9039918]

Pettersen EF, Goddard TD, Huang CC, Couch GS, Greenblatt DM, Meng EC, and Ferrin TE (2004). UCSF Chimera--a visualization system for exploratory research and analysis. J Comput Chem 25, 1605–1612. [PubMed: 15264254]

Phillips DD, Fattah RJ, Crown D, Zhang Y, Liu S, Moayeri M, Fischer ER, Hansen BT, Ghirlando R, Nestorovich EM, et al. (2013). Engineering anthrax toxin variants that exclusively form octamers and their application to targeting tumors. J Biol Chem 288, 9058–065. [PubMed: 23393143]

Pohanka M (2019). Current Trends in the Biosensors for Biological Warfare Agents Assay. Materials (Basel) 12.

Punjani A, Rubinstein JL, Fleet DJ, and Brubaker MA (2017). cryoSPARC: algorithms for rapid unsupervised cryo-EM structure determination. Nat Methods 14, 290–296. [PubMed: 28165473]

Rohou A, and Grigorieff N (2015). CTFFIND4: Fast and accurate defocus estimation from electron micrographs. J Struct Biol 192, 216–221. [PubMed: 26278980]

Santelli E, Bankston LA, Leppla SH, and Liddington RC (2004). Crystal structure of a complex between anthrax toxin and its host cell receptor. Nature 430, 905–908. [PubMed: 15243628]

Scheres SH (2012). RELION: implementation of a Bayesian approach to cryo-EM structure determination. J Struct Biol 180, 519–530. [PubMed: 23000701]

Shen Y, Zhukovskaya NL, Guo Q, Florian J, and Tang WJ (2005). Calcium-independent calmodulin binding and two-metal-ion catalytic mechanism of anthrax edema factor. EMBO J 24, 929–941. [PubMed: 15719022]

Swint-Kruse L, and Brown CS (2005). Resmap: automated representation of macromolecular interfaces as two-dimensional networks. Bioinformatics 21, 3327–3328. [PubMed: 15914544]

Thoren KL, and Krantz BA (2011). The unfolding story of anthrax toxin translocation. Mol Microbiol 80, 588–595. [PubMed: 21443527]

Wickner W, and Schekman R (2005). Protein translocation across biological membranes. Science 310, 1452–1456. [PubMed: 16322447]

Wynia-Smith SL, Brown MJ, Chirichella G, Kemalyan G, and Krantz BA (2012). Electrostatic ratchet in the protective antigen channel promotes anthrax toxin translocation. J Biol Chem 287, 43753–43764. [PubMed: 23115233]

Zhang S, Udho E, Wu Z, Collier RJ, and Finkelstein A (2004). Protein translocation through anthrax toxin channels formed in planar lipid bilayers. Biophys J 87, 3842–3849. [PubMed: 15377524]

Zheng SQ, Palovcak E, Armache JP, Verba KA, Cheng Y, and Agard DA (2017). MotionCor2: anisotropic correction of beam-induced motion for improved cryo-electron microscopy. Nat Methods 14, 331–332. [PubMed: 28250466]

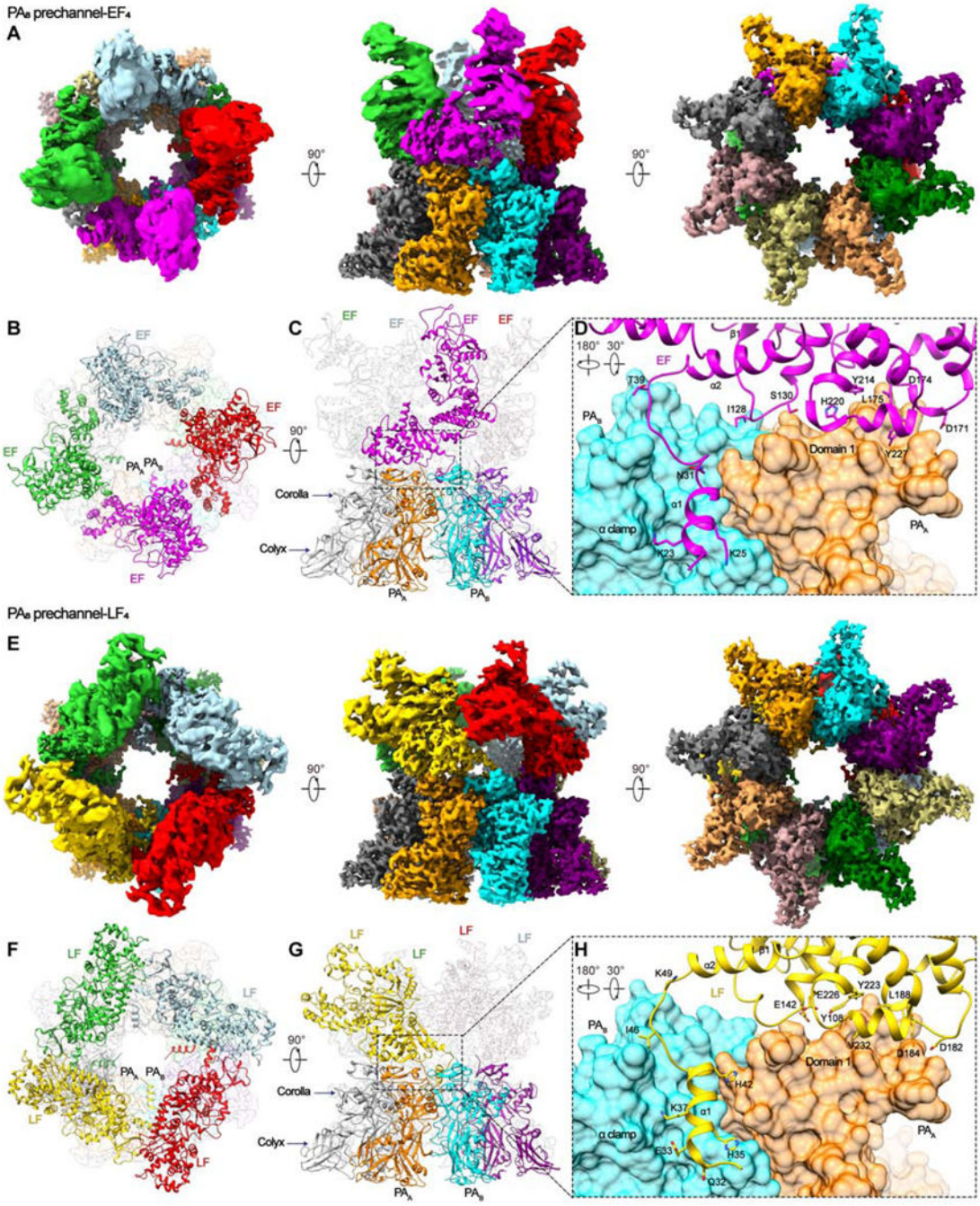

Figure 1. CryoEM density maps and atomic models of PA_8 prechannel-EF complex (PA_8 prechannel-EF_4) and PA_8 prechannel-LF complex (PA_8 prechannel-LF_4).

(A) Top (left panel), side (middle panel) and bottom (right panel) views of the PA_8 prechannel-EF_4 cryoEM density map colored by subunits. **(B)** Ribbon representation of the PA_8 prechannel-EF_4 structure as viewed from the top and side like in left panel of (A). The four EF subunits are colored differently and the eight PA subunits are shown in light shade. **(C)** Ribbon representation of the PA_8 prechannel-EF_4 structure as viewed from the side like in middle panel of (A). One of the four EF subunits is colored while the others are in a light

shade; four PA subunits are colored with the remaining ones in a light shade. **(D)** Details of the interactions between an EF subunit and two neighboring PA subunits. **(E)** Top (left panel), side (middle panel) and bottom (right panel) views of the PA_8 prechannel-LF_4 cryoEM density map colored by subunits. **(F)** Ribbon representation of the PA_8 prechannel-LF_4 structure as viewed from the top like in left panel of (E). **(G)** Ribbon representation of the PA_8 prechannel-LF_4 structure as viewed from the side like in middle panel of (E). **(H)** Details of the interactions between an LF subunit and two neighboring PA subunits. See also Figures S1, S2 and S3.

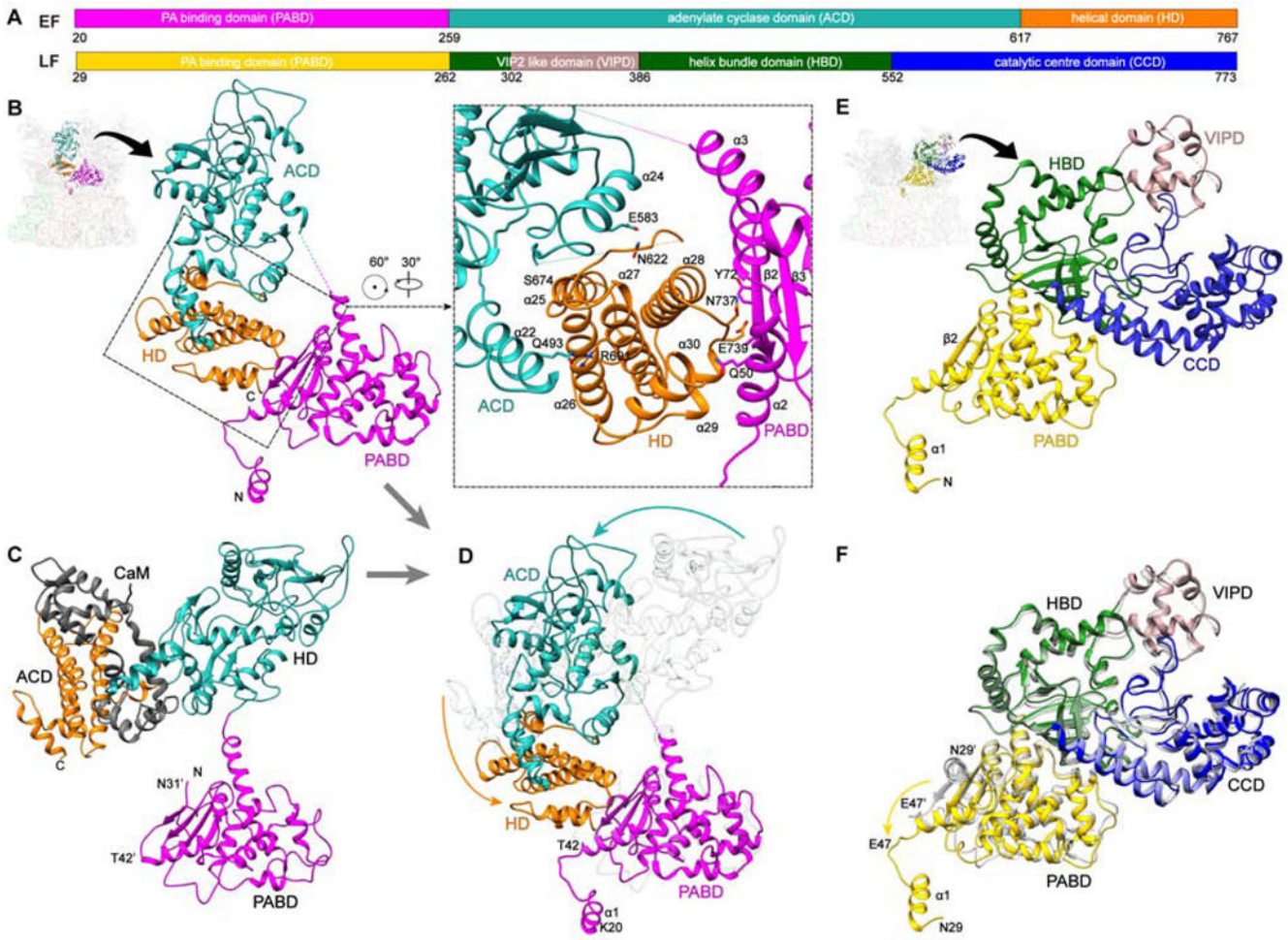

Figure 2. Structural comparisons of PA-bound and PA-free enzyme factors.

(A) Domains of EF and LF with boundary residues numbered. **(B-D),** Structure of PA_8 prechannel-bound EF. One PA-bound EF subunit is colored by domains (B) alongside the CaM-bound EF (C). These two structures are then superposed by aligning their PABDs to show the movements of both ACD and HD upon binding to PA_8 prechannel (D). In (D), the domains in the CaM-bound EF are light shaded. **(E** and **F),** Structure of PA-bound LF (E) and its superposition with apo-LF structure (F) (PDB: 1J7N). See also Figure S4.

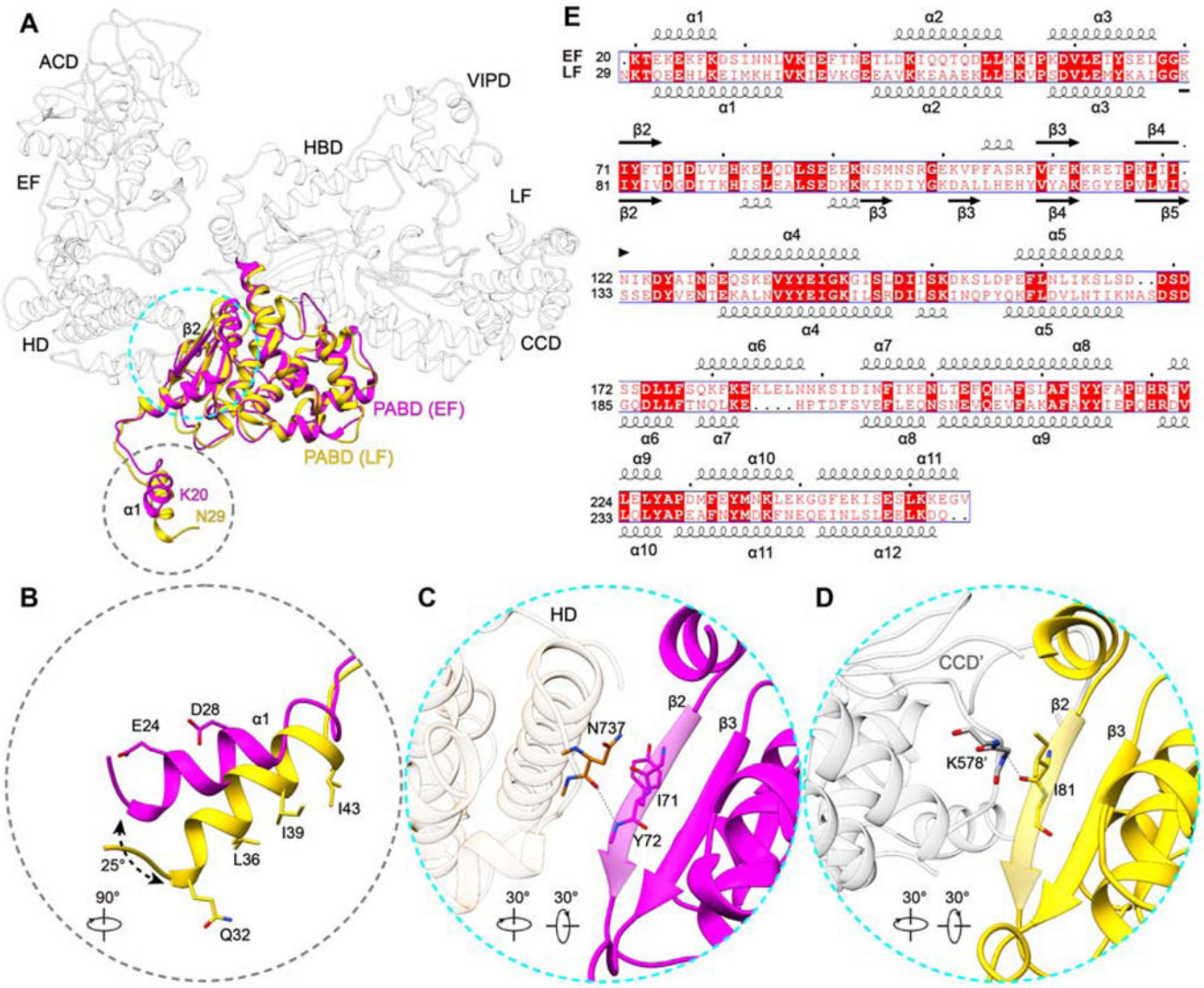

Figure 3. Structural comparison of EF and LF bound to PA_8 prechannel.

(A-D), Superposition of PA_8 prechannel-bound EF and PA_8 prechannel-bound LF structures after aligning their PABDs (A) with close-ups showing differences in the α1 helix (B) and β2 interactions (C and D). **(E)** Sequence alignment of PABDs of EF and LF with their secondary structure elements indicated.

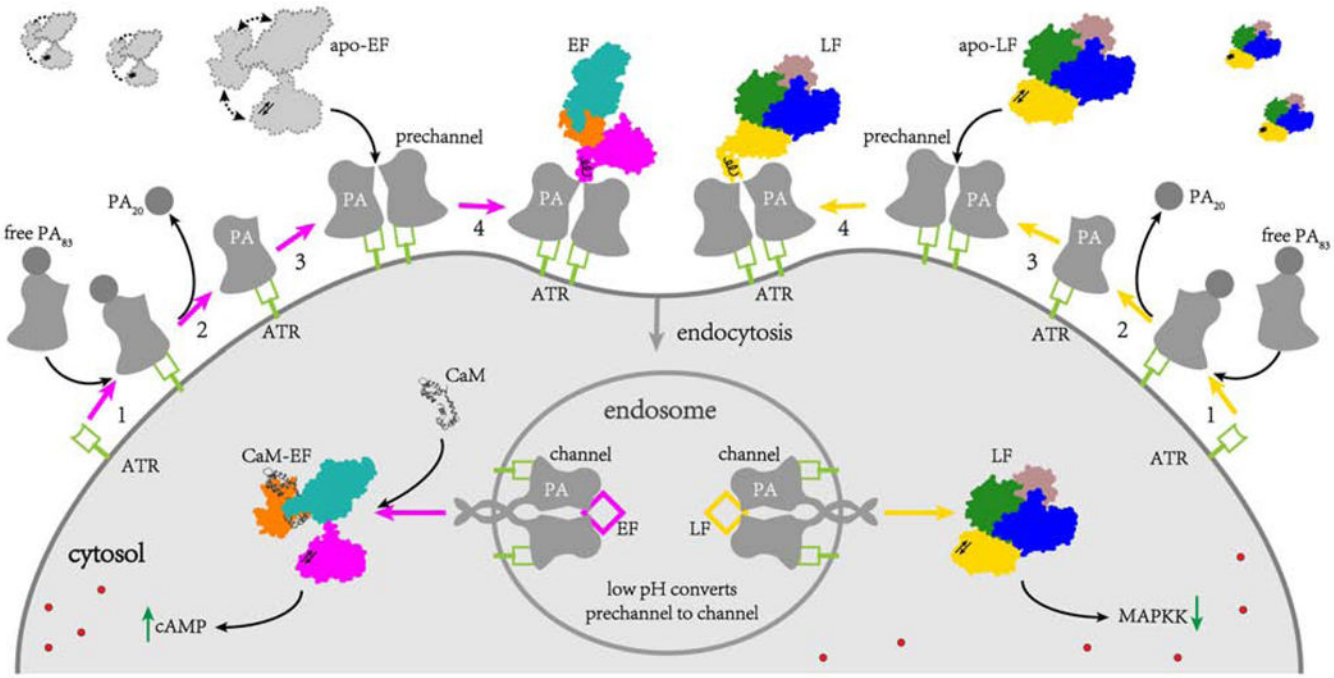

Figure 4. Pre-translocation illustration of the anthrax toxins in multiple steps.

Step 1: PA_{83} binds an anthrax toxin receptor. **Step 2**: Protease cleaves PA_{83} to PA_{63} (PA) and a small 20 kD fragment. **Step 3:** PA assembles into a heptamer or octamer prechannel. **Step 4:** Along with conformational changes, EF and LF bind to the PA prechannel. For simplicity, only two PA subunits in prechannel or channel are depicted.

KEY RESOURCES TABLE

Reagent or Resource	Source	Identifier
Bacterial and Virus Strains		
E. coli BL21(DE3)	Thermo Fisher	Cat# EC0114
Recombinant DNA		
pET22b vector	Novagen	Cat# 69744-3
pET15b vector	Novagen	Cat# 69661-1
Critical Commercial Assays		
QuikChange II XL site-directed mutagenesis kits	Agilant	Cat# 200251
Deposited Data		
Crystal structure of CaM-bound EF	(Shen et al., 2005)	PDB: 1XFY
Crystal structure of apo LF	(Pannifer et al., 2001)	PDB: 1J7N
Crystal structure of PA_8 prechannel octamer	(Kintzer et al., 2009)	PDB: 3HVD
CryoEM structure of PA_8 prechannel in complex with EF	This study	PDB: 6VRA EMDB: EMD-21365
CryoEM structure of PA_8 prechannel in complex with LF	This study	PDB: 6WJJ EMDB: EMD-21694
Chemicals, Peptides, and Recombinant Proteins		
3C Protease	Thermo Fisher	Cat# 88946
Software and Algorithms		
MotionCor2	(Zheng et al., 2017)	https://emcore.ucsf.edu/ucsf-motioncor2
Resmap	(Swint-Kruse and Brown, 2005)	http://resmap.sourceforge.net/
RELION	(Scheres, 2012)	https://www3.mrc-lmb.cam.ac.uk/relion/index.php/Main_Page
Continued		
SerialEM	(Mastronarde, 2005)	https://bio3d.colorado.edu/SerialEM/
CTFFIND4	(Rohou and Grigorieff, 2015)	https://grigoriefflab.umassmed.edu/ctffind4
Gautomatch	N/A	http://www.mrc-lmb.cam.ac.uk/kzhang
cryoSPARC	(Punjani et al., 2017)	https://cryosparc.com/
Coot	(Emsley and Cowtan, 2004)	https://www2.mrclmb.cam.ac.uk/personal/pemsley/coot/
Phenix	(Adams et al., 2010)	
UCSF Chimera	(Pettersen et al., 2004)	https://www.cgl.ucsfedu/chimera/
UCSF ChimeraX	(Goddard et al., 2018)	https://www.cgl.ucsfedu/chimerax/
Other		
QUANTIFOIL® R 2/1 grids	TED PELLA	Cat# 661-300-CU